

Article

Metal–Organic Framework Derived Ni₂P/FeP@NPC Heterojunction as Stability Bifunctional Electrocatalysts for Large Current Density Water Splitting

Huimin Jiang ¹, Shuo Zhang ¹, Qiuju Fu ¹, Liting Yan ² , Jun Zhang ^{1,*} and Xuebo Zhao ^{1,2,*} 

¹ State Key Laboratory of Heavy Oil Processing, College of Chemistry and Chemical Engineering, China University of Petroleum (East China), Qingdao 266580, China

² School of Materials Science and Engineering, Qilu University of Technology (Shandong Academy of Sciences), Jinan 250353, China

* Correspondence: zhangj@upc.edu.cn (J.Z.); zhaoxuebo@upc.edu.cn (X.Z.)

Abstract: The construction of heterojunction has been widely accepted as a prospective strategy for the exploration of non-precious metal-based catalysts that possess high-performance to achieve electrochemical water splitting. Herein, we design and prepare a metal-organic framework derived N, P-doped-carbon-encapsulated Ni₂P/FeP nanorod with heterojunction (Ni₂P/FeP@NPC) for accelerating the water splitting and working stably at industrially relevant high current densities. Electrochemical results confirmed that Ni₂P/FeP@NPC could both accelerate the hydrogen and oxygen evolution reactions. It could substantially expedite the overall water splitting (1.94 V for 100 mA cm⁻²) which is close to the performance of RuO₂ and the Pt/C couple (1.92 V for 100 mA cm⁻²). In particular, the durability test exhibited that Ni₂P/FeP@NPC delivers 500 mA cm⁻² without decay after 200 h, demonstrating the great potential for large-scale applications. Furthermore, the density functional theory simulations demonstrated that the heterojunction interface could give rise to the redistribution of electrons, which could not only optimize the adsorption energy of H-containing intermediates to achieve the optimal ΔG_H^{*} in a hydrogen evolution reaction, but also reduce the ΔG value in the rate-determining step of an oxygen evolution reaction, thus improving the HER/OER performance.

Keywords: metal-organic frameworks; heterojunction; electrocatalysis; large current density; water splitting



Citation: Jiang, H.; Zhang, S.; Fu, Q.; Yan, L.; Zhang, J.; Zhao, X.

Metal–Organic Framework Derived Ni₂P/FeP@NPC Heterojunction as Stability Bifunctional Electrocatalysts for Large Current Density Water Splitting. *Molecules* **2023**, *28*, 2280. <https://doi.org/10.3390/molecules28052280>

Academic Editor: Antonella Curulli

Received: 12 January 2023

Revised: 6 February 2023

Accepted: 21 February 2023

Published: 28 February 2023



Copyright: © 2023 by the authors. Licensee MDPI, Basel, Switzerland. This article is an open access article distributed under the terms and conditions of the Creative Commons Attribution (CC BY) license (<https://creativecommons.org/licenses/by/4.0/>).

1. Introduction

Electrocatalytic overall water splitting exhibits great potential in sustainable hydrogen production, which is composed of two half reactions, one being a hydrogen evolution reaction (HER) and the other being an oxygen evolution reaction (OER) [1,2]. However, the efficiency of water splitting has been strongly hindered by the sluggish kinetics process [3]. Previous reports have proved that the traditional noble metal-based electrocatalysts have high catalytic performance on HER or OER, such as iridium and ruthenium oxides for OER and platinum for HER [4,5]. However, these catalysts might only be suitable for the half reaction, and commonly suffer from expensive costs and scarce reserves. In general, several requirements must be met for water splitting catalysts to achieve practical applications: (1) stable and high active sites at large current density [6]; (2) fast electron transfer [7]; and (3) low-cost and easy access [8]. Recently, some progress was achieved in electrochemical water splitting; nevertheless, most of the reported electrodes were evaluated in terms of overpotentials and stability at low current densities, which are not practical for large-scale applications [9]. It remains an urgent need to explore high-performance catalysts with large current density and robust durability for overall water splitting [3,10]. The development of non-noble metal bifunctional electrocatalysts with robust and stable catalytic performance

has exhibited great potential in practical applications, and the exploration of bifunctional catalysts with both HER and OER will significantly simplify the water splitting devices.

Currently, tremendous efforts have been made in developing efficient and scalable overall water splitting electrocatalysts [11,12]. It has been established that the transition metal phosphides, such as Fe and Ni-based phosphides, possess superior electrical conductivity and high electron density near the Fermi level. They can effectively improve the intrinsic conductivity of materials to realize large charge carrier transfer efficiency and catalytic capability in the electrocatalytic process [13,14]. The positively charged metal cations in metal phosphides can be regarded as the hydroxyl receptors, and negatively charged phosphorous active sites can accelerate the dissociation of H_2 to boost HER activity. Furthermore, the introduction of secondary metal into the metal center can increase the active sites, optimize the e_g orbitals, change the charge transfer path, and modulate the electronic structure for better electrocatalytic capabilities in overall water splitting [15]. To date, however, the uncontrolled generation of multiple segregated phases due to the reactive difference of metal centers still makes it challenging to synthesize homogeneous bimetallic phosphides.

As a new class of crystalline materials, metal-organic frameworks (MOFs) are constructed with metal nodes and organic ligands [16–18]. Their compositions and chemical environments can be easily modulated and systematically designed via changes of metal ions in the MOF precursor, or by annealing processes in various environments [19]. In addition, the structure and morphology of the obtained products can be well preserved [20,21]. For now, numerous different functional MOFs have been created by changing the metal ions/clusters and organic linkers which have been regarded as promising candidates for carbon-based materials [22,23].

In this work, we report the designing and fabricating of Ni_2P/FeP heterojunction encapsulated in N, P-doped carbon frameworks (denoted as $Ni_2P/FeP@NPC$) through a bimetallic MOF precursor topochemical conversion, aiming at boosting both the activity and durability of OER and HER electrocatalysts. First, we synthesized the Ni/Fe MOF, which was then followed by pyrolysis, and the phosphating of the $Ni_2P/FeP@NPC$ was conducted. Because of the remarkable HER and OER activity, this bifunctional $Ni_2P/FeP@NPC$ was integrated in an alkaline electrolyzer as both the anode and cathode electrodes. The experimental results demonstrated that only a cell voltage of 1.64 V could deliver 10 mA cm^{-2} , and a cell voltage of 2.37 V was needed to deliver 500 mA cm^{-2} with 200 h durability, outperforming most catalysts with similar functions and those of precious metal catalysts (Pt/C// RuO_2 , 2.41 V for 500 mA cm^{-2}).

2. Results and Discussion

The synthetic step of the $Ni_2P/FeP@NPC$ catalysts is illustrated in Figure 1a. The MOFs precursors (denoted as STA-12) were prepared with a hydrothermal method according to previous work with small modifications (all details can be obtained from the Supporting information) [24]. The metal nodes in STA-12 were tailored by adjusting the species of metal salts in the preparation process. As shown in Figure 1b, the powder X-ray diffraction (PXRD) patterns demonstrated that all STA-12 crystals possessed the same PXRD pattern and exhibited high agreement with the reference [24], which confirmed that the bimetallic STA-12 crystals possessed the same crystal structure with single-metal-center STA-12. The scanning electron microscopy images (SEM) in Figure 1c–e show that all the STA-12 exhibited similar regular nanorod morphologies. Interestingly, as shown in Figure 1e, compared with single-metal-center STA-12, the bimetallic STA-12-FeNi exhibited much slender morphologies, which might be caused by the presence of Fe that caused the MOF crystal growing along specific lattice plane, limiting the growth in other lattice planes.

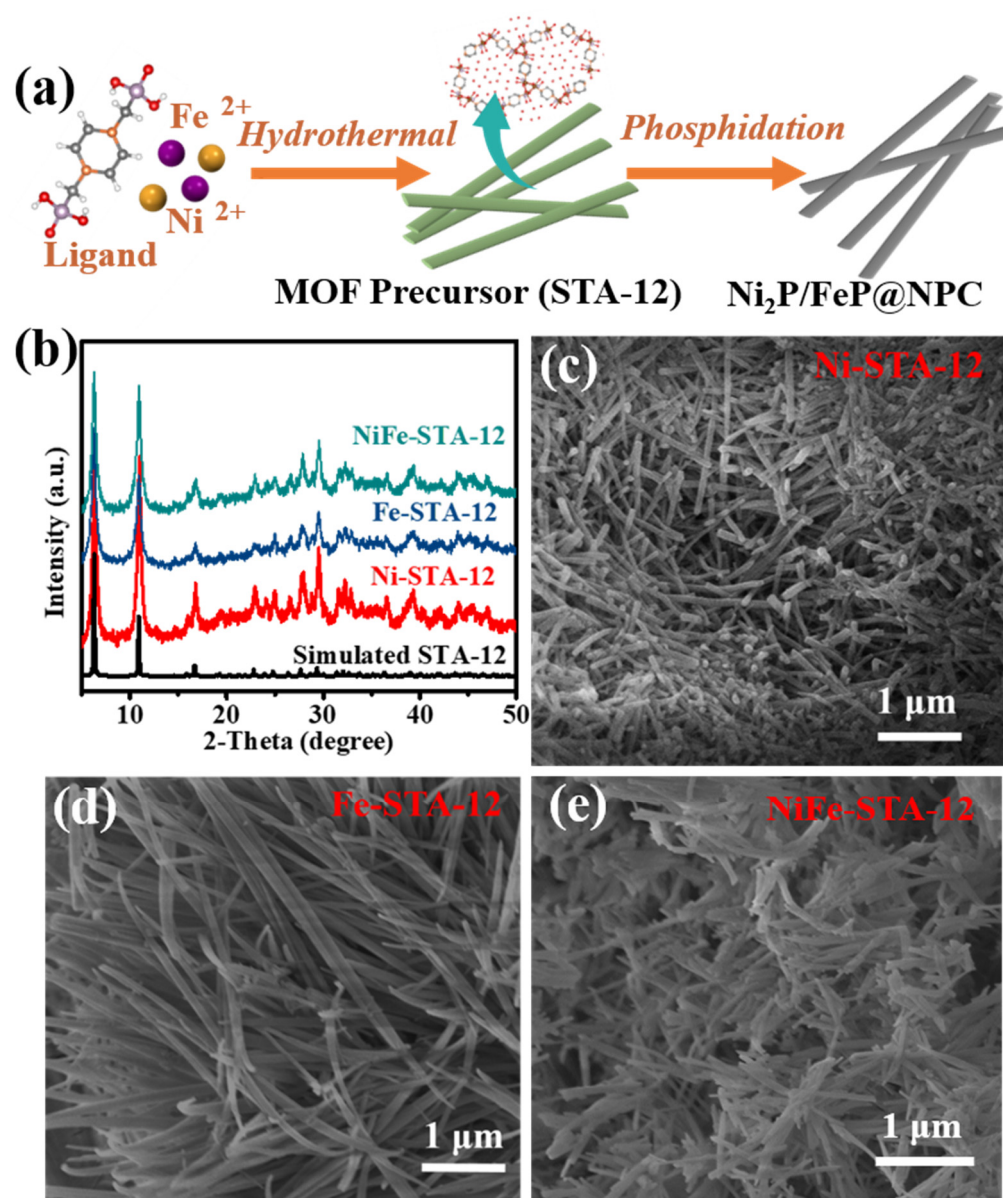


Figure 1. (a) Synthetic routes in the schematic illustration of the MOF precursor and the derived $\text{Ni}_2\text{P}/\text{FeP}@NPC$; (b) XRD patterns of the obtained MOFs; (c–e) are the SEM images of Ni-STA-12, Fe-STA-12, and NiFe-STA-12, respectively.

After carbonization and phosphorization of the MOF precursor, the XRD patterns of $\text{Ni}_2\text{P}@NPC$, $\text{FeP}@NPC$, and $\text{Ni}_2\text{P}/\text{FeP}@NPC$ are shown in Figure 2a. The peaks at 2θ of 31.83° , 35.33° , 40.75° , 44.64° , 54.15° and 54.37° are matched well with hexagonal Ni_2P crystal planes (JCPDS No. 65-3544) of (011), (111), (021), (210), (300) and (002), respectively. Meanwhile, the peaks of FeP at 2θ of 32.78° , 37.18° , 46.32° , 46.98° , 48.36° , 56.09° are also illustrated, which belong to the (011), (111), (112), (202), (211) and (212) crystal planes respectively, and exhibited high agreement with orthorhombic FeP (JCPDS No. 65-2595). As shown in Figure S1, the obtained Raman spectrums of the all catalysts exhibited two broad and obvious peaks positioned at 1355 and 1603 cm^{-1} corresponding to the typical D and G bands of graphene, respectively. The detection of these two peaks demonstrated the existence of substantial defects or disordered sites, which might be due to the concurrent doping and absence of C atoms. The SEM images were then collected to explore the morphology of the materials after the carbonization of MOF precursors (Figures 2b and S2). It can be seen that the morphology of $\text{Ni}_2\text{P}@NPC$, $\text{Ni}_2\text{P}/\text{FeP}@NPC$ and

FeP@NPC are similar to the MOF precursors, indicating that the morphology can be well preserved during the phase transformation process. As shown in Figure 2c, the transmission electron microscopy (TEM) image exhibited that Ni₂P/FeP@NPC possessed a typical rod-shaped morphology with a diameter of approximately 120 nm. From high-resolution TEM (HRTEM) images (Figure 2d), lattice fringes could be observed in the Ni₂P/FeP@NPC, in which the spacing of 0.204 nm was attributed to the (021) planes of Ni₂P. In contrast, the lattice fringe with an inter-planar distance of 0.193 nm was corresponding to the (220) crystal planes of FeP. All of these results exhibited high consistency with the XRD analysis, proving the successful preparation of Ni₂P/FeP@NPC. As shown in Figure 2d, the obvious phase boundary between the marked Ni₂P and FeP proved the production of a heterostructure, which could generate an interfacial bonding effect that facilitates the exposure of more active sites. Furthermore, the lattice fringe with a spacing distance of 0.34 nm could be ascribed to the (002) plane of graphitic carbon, confirming the existence of carbon substrate through the pyrolysis process. The energy-dispersive X-ray spectrometry (EDX) mapping was applied to reveal the element distribution of Ni₂P/FeP. As shown in Figure S3, the elements of C, Ni, Fe, P, and N are homogeneously dispersed in the structures, demonstrating the successful preparation of Ni₂P/FeP@NPC compounds.

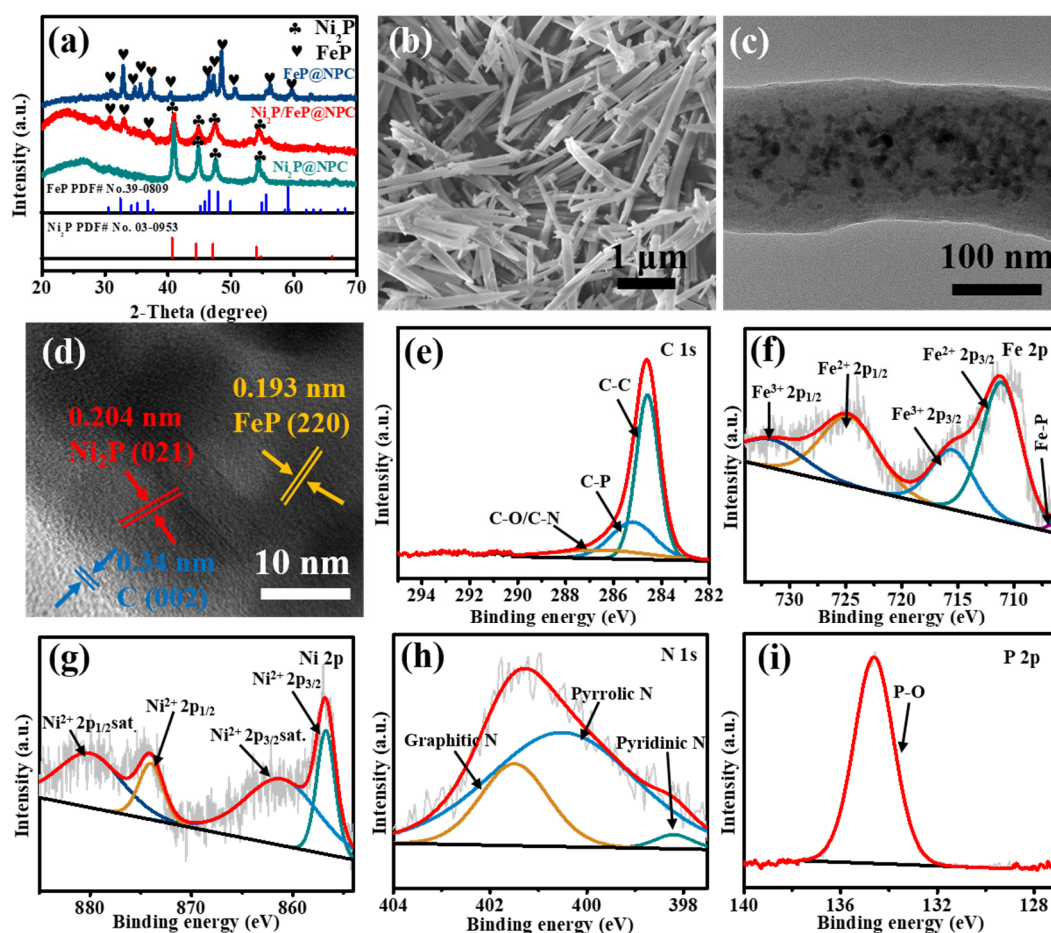


Figure 2. (a) XRD pattern of Ni₂P@NPC, Ni₂P/FeP@NPC and FeP@NPC; (b) SEM images of Ni₂P/FeP@NPC; (c) TEM images of Ni₂P/FeP@NPC; (d) HRTEM image of Ni₂P/FeP@NPC; High-resolution XPS spectra of (e) C, (f) Fe (g) Ni, (h) N and (i) P in Ni₂P/FeP@NPC.

X-ray photoelectron spectroscopy (XPS) was employed to evaluate the valence state and composition of the prepared samples more accurately. The XPS survey scan spectrum in Figure S4 indicated the existence of C, Fe, Ni, N, and P in the architecture. The high-resolution spectra of these elements further confirmed the formation of Ni₂P/FeP@NPC.

The C 1s XPS spectrum in Figure 2e could be deconvoluted into three peaks positioned at 286.5, 285.2, and 284.6 eV, which were ascribed to the C-O/C-N, C-P, and C-C/C = C groups, respectively [25]. The existence of C-O, C-P, and C-N offered numerous anchoring sites for electrochemically active materials to inhibit agglomeration or disengagement of particles from electrodes. As shown in Figure 2f, two main spin-orbit doublets in the Fe 2p spectrum could be divided into four components: the first doublet located at 711.1 eV and 724.6 eV belonged to Fe^{2+} 2p_{3/2} and Fe^{2+} 2p_{1/2}, and the second doublet located at 715.5 eV and 731.6 eV was ascribed to the splitting peaks of Fe^{3+} 2p_{3/2} and Fe^{3+} 2p_{1/2}, respectively. In addition, the small peak positioned at 706.7 eV indicated the existence of metallic Fe [26]. As shown in Figure 2g, the two spin-orbit doublet peaks at 856.7 and 874.0 eV with two shake-up satellites at 861.1 and 880.0 eV indicated the existence of oxidized Ni species in Ni₂P/FeP@NPC, ascribed to the surface oxidation in air [27]. As shown in Figure 2h, the peak located at 133.7 eV in the P 2p region was attributed to the oxidized phosphide (P-O) [26]. Furthermore, the N 1s spectrum in Figure 2i could be deconvoluted into pyridinic-N (398.2 eV), pyrrolic-N (400.5 eV), and quaternary-N (401.5 eV), confirming the incorporation of N into Ni₂P/FeP@NPC. Previous reports have proved that the incorporation of the N species in the catalysts could efficiently improve the intrinsic electrocatalytic activities, which could effectively improve the catalytic performance [28]. All of these results demonstrated that Ni₂P/FeP@NPC catalysts with the combination of conductive N, P-doped carbon and highly active Ni₂P/FeP heterostructures have been established.

The catalytic performance of the Ni₂P/FeP@NPC hybrid catalyst was then investigated. Firstly, the OER activity of the Ni₂P/FeP@NPC catalysts in 1.0 M KOH electrolyte was investigated. As shown in Figure 3a, the representative polarization curves exhibited the geometric current density plotted against applied potential vs the reversible hydrogen electrode (RHE) of this Ni₂P/FeP@NPC catalyst. The OER activities of Ni₂P@NPC, FeP@NPC, and RuO₂ were also evaluated by the same procedure. As shown in Figure 3a, Ni₂P@NPC and FeP@NPC show larger overpotential of 621 and 699 mV at 400 mA cm⁻², respectively, while Ni₂P/FeP@NPC exhibited a much higher OER catalytic activity possessing the overpotential of 487 mV under the same condition. Specifically, the OER activities of other available bifunctional catalysts were compared with Ni₂P/FeP@NPC in Figure 3b and Table S1. Experimental results exhibited that the catalyst in this work required the lowest overpotential of 273 mV to achieve 10 mA cm⁻², indicating the potential application in overall water splitting at the small cell voltage. The OER kinetics of Ni₂P/FeP@NPC was further investigated by the Tafel slope to disclose the inherent property of catalysts. As shown in Figure 3c, the measured Tafel slopes of Ni₂P/FeP@NPC was 79 mV dec⁻¹, was considerably lower than the counterparts of FeP (93 mV dec⁻¹), RuO₂ (105 mV dec⁻¹), and Ni₂P (88 mV dec⁻¹). The much smaller Tafel slopes of Ni₂P/FeP@NPC revealed the favorable OER kinetics of Ni₂P/FeP@NPC. Electrochemical impedance spectroscopy (EIS) measurements of Ni₂P@NPC, Ni₂P/FeP@NPC and FeP@NPC in Figure 3d were conducted at OER conditions to reveal the charge transfer kinetics. The semicircle of Ni₂P/FeP@NPC is much smaller than that of Ni₂P@NPC and FeP@NPC, demonstrating that the bimetallic phosphide Ni₂P/FeP@NPC possessed smaller charge transfer resistance. The electrochemically active surface area values of catalysts were further investigated by double-layer capacitances (C_{dl}), which were obtained by calculating the CV curves at different scan rates (Figures S5–S7). As shown in Figure 3e, the C_{dl} values of Ni₂P/FeP@NPC (5.35 mF cm⁻²) are much higher than those of Ni₂P (0.60 mF cm⁻²) and FeP (1.12 mF cm⁻²), demonstrating the higher exposed catalytic sites of Ni₂P/FeP@NPC. Stability is another important indicator of electrocatalysts for practical applications. We further explored the stability of Ni₂P/FeP@NPC by the long-term cycling test and amperometric i-t measurement. As illustrated in Figure 3f, the polarization curve of Ni₂P/FeP@NPC after 10,000 CV cycles almost overlaps with the initial curve. Furthermore, the Ni₂P/FeP@NPC maintained good stability for 100 h at 500 mA cm⁻² (Figure 3g), which proves the long-term durability of Ni₂P/FeP@NPC under large current density.

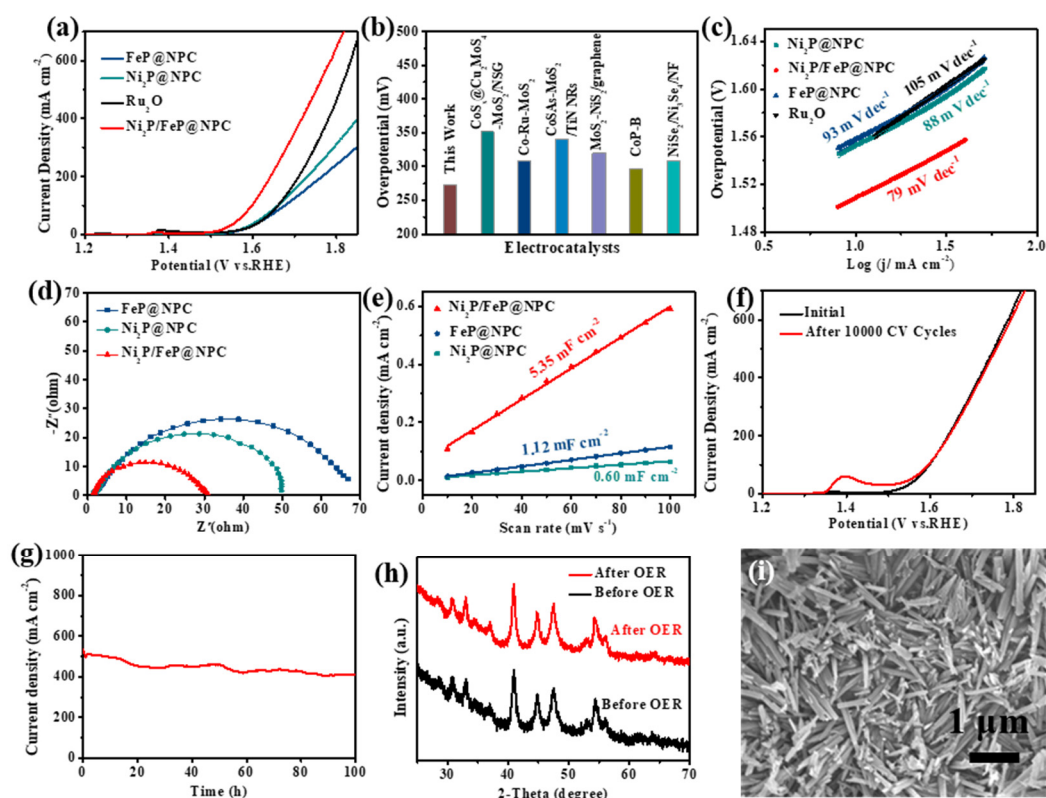


Figure 3. (a) The OER polarization curves of different catalysts in 1.0 M KOH solution; (b) Comparison of the overpotentials obtained at 10 mA cm^{-2} among $\text{Ni}_2\text{P}/\text{FeP}@NPC$ and other reported OER catalysts (references are provided in Table S1); (c) The relevant Tafel plots of different catalysts; (d) Nyquist plots of different catalysts; (e) Double-layer capacitance measurements to calculate the electrochemically active surface areas; (f) OER LSV curves of $\text{Ni}_2\text{P}/\text{FeP}@NPC$ before (black) and after (red) 10,000 CV cycles; (g) The chronopotentiometry curves of the $\text{FeP}/\text{Ni}_2\text{P}$ electrode after 100 h examination; (h) PXRD pattern, and (i) SEM image of $\text{Ni}_2\text{P}/\text{FeP}@NPC$ after chronoamperometric measurements for OER.

Because of the fantastic OER durability of $\text{Ni}_2\text{P}/\text{FeP}@NPC$, we further tried to investigate the origin of OER performance. XRD, SEM and XPS were used to study the characteristics of $\text{Ni}_2\text{P}/\text{FeP}@NPC$ after OER stability testing (at the current density of 500 mA cm^{-2} for 100 h). As shown in Figure 3h, the XRD pattern of $\text{Ni}_2\text{P}/\text{FeP}@NPC$ did not change obviously after OER, implying that the crystal structure remained unchanged. Meanwhile, the morphology of the sample after OER was tested and presented in Figure 3i. It can be concluded that the $\text{Ni}_2\text{P}/\text{FeP}@NPC$ maintained its morphology and dimension after the stability testing, demonstrating the excellent corrosion resistance and chemical stability of $\text{Ni}_2\text{P}/\text{FeP}@NPC$. XPS was further utilized to evaluate the change in the surface chemical composition and the electronic state after the catalytic process. The XPS spectrum after initial OER in Figure S8 exhibited the presence of Ni, Fe, C, P and N elements in the catalysts. The corresponding peaks of C, Fe, Ni, N and P in the high-resolution XPS spectrum exhibited little change with the appearance of the peak attributed to $\text{O}=\text{C}-\text{O}$ (292.1 eV) (Figure S8b–f), suggesting the slight surface oxidation of $\text{Ni}_2\text{P}/\text{FeP}@NPC$. The result agreed with XRD analysis, which proved that the N, P-doped carbon could effectively prevent the $\text{Ni}_2\text{P}/\text{FeP}$ from degradation, oxidation and corrosion during the OER. Therefore, the real active sites of $\text{Ni}_2\text{P}/\text{FeP}@NPC$ electrocatalyst for OER were the combination of N, P-doped carbon, and the $\text{Ni}_2\text{P}/\text{FeP}$ heterostructures.

Next, we further explored the possibility of $\text{Ni}_2\text{P}/\text{FeP}@NPC$ as a HER catalyst. As shown in Figure 4a, $\text{Ni}_2\text{P}/\text{FeP}@NPC$ exhibited considerable HER catalytic activity with low overpotentials of 182 mV to obtain the current density of 10 mA cm^{-2} , while the much

higher overpotentials of 217 and 214 mV were needed to achieve the current density of 10 mA cm^{-2} for FeP@NPC and Ni₂P@NPC, respectively. Moreover, the calculated Tafel slope of Ni₂P/FeP@NPC in Figure 4b was 85 mV dec^{-1} , which was smaller than those of Ni₂P (126 mV dec^{-1}) and FeP (144 mV dec^{-1}), indicating that Ni₂P/FeP@NPC possessed the fastest HER kinetic process. Moreover, EIS was also conducted to evaluate the intrinsic HER electrocatalytic kinetics. The corresponding Rct of Ni₂P/FeP@NPC was smaller than those of Ni₂P@NPC and FeP@NPC, demonstrating the higher transfer coefficient and electronic conductivity (Figure 4c). Furthermore, the Ni₂P/FeP@NPC catalyst possessed excellent stability during long-time HER operations. As shown in Figure 4d, the catalytic performance exhibited no apparent deterioration after 10,000 cycles. As shown in Figure 4e, Ni₂P/FeP@NPC maintained the current density of 400 mA cm^{-2} for 100 h without obvious decline, demonstrating the fantastic durability of Ni₂P/FeP@NPC in the HER process. Such excellent HER durability of Ni₂P/FeP@NPC ranks at the top level of the reported HER electrocatalysts.

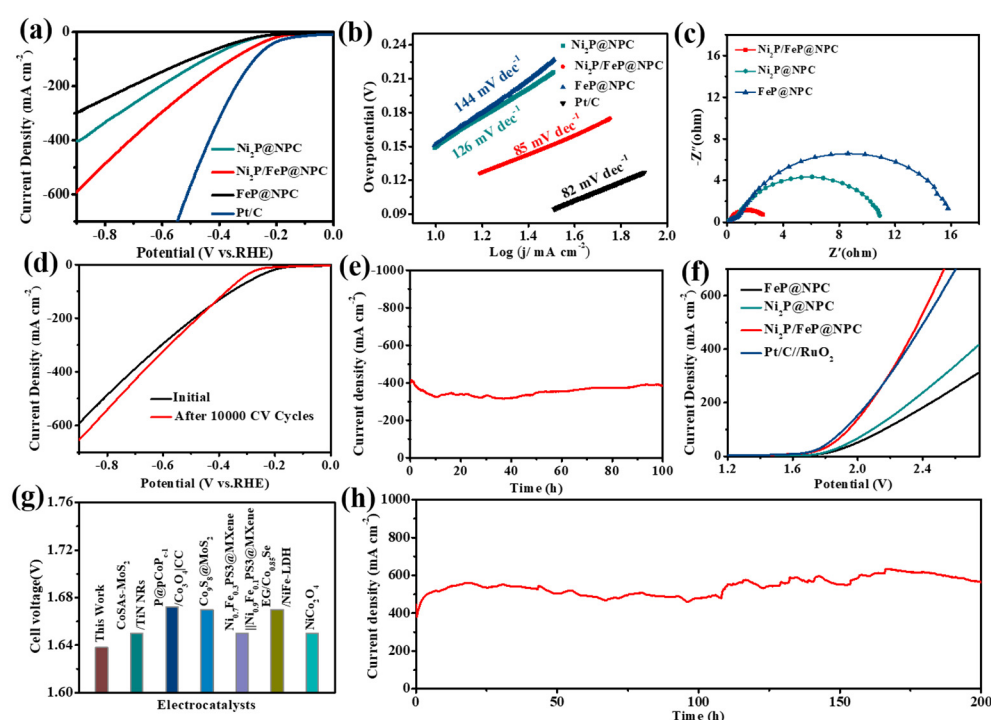
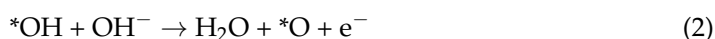


Figure 4. (a) The HER polarization curves of different catalysts; (b) The relevant Tafel plots of different catalysts; (c) Nyquist plots of different catalysts; (d) HER LSV curves of Ni₂P/FeP@NPC before (black) and after (red) 10,000 CV cycles; (e) The chronopotentiometry curve of the Ni₂P/FeP@NPC electrode tested for 100 h. (f) The polarization curves of different catalysts for overall water splitting. (g) Comparison of the potentials required at 10 mA cm^{-2} among Ni₂P/FeP@NPC and the available reported catalysts for overall water splitting (References are provided in Table S2); (h) The chronopotentiometric curve of the Ni₂P/FeP@NPC electrode tested at the constant current density of 500 mA cm^{-2} for 200 h.

Because of the fantastic catalytic activity of Ni₂P/FeP@NPC for HER and OER, the two-electrode water splitting device was constructed using Ni₂P/FeP@NPC as the bifunctional catalyst for HER and OER. Remarkably, the cell voltage to afford the current density of 10 mA cm^{-2} was low to 1.64 V (Figure 4f), which was comparable to the coupled benchmark RuO₂//Pt/C catalysts (1.63 V), and better than many previously reported bifunctional electrocatalysts (Figure 4g and Table S2). In addition, as shown in Figure 4h, the device exhibited outstanding stability for 200 h after the long-term test at the current density of 500 mA cm^{-2} .

To clarify the interfacial charge properties, theoretical models of Ni₂P@NPC, FeP@NPC, and Ni₂P/FeP@NPC heterostructures were established (Figure S9) and DFT calculations were utilized to evaluate their surface energetics. Figure 5a shows the differential charge density between N, P-doped carbon and Ni₂P/FeP in the heterostructure. Yellow and cyan refer to the positive and negative charges, respectively. As shown in Figure 5a, the differential charge density at the Ni₂P/FeP@NPC interface indicated that the significant electron redistribution was achieved through the extensive electron transformation from the Ni₂P/FeP side to the NPC region. Thus, the NPC side was electron accumulating, whereas the Ni₂P/FeP domain was electron depleting, which indicated the strong electronic interaction between these two domains. This kind of interfacial electronic structure was beneficial for the surface adsorption of the intermediate. As shown in Figure 5b, the density of states (DOS) was further conducted to evaluate their electrical conductivity. The results showed that the Ni₂P/FeP@NPC possessed higher carrier density around the Fermi level compared with Ni₂P@NPC and FeP@NPC, which demonstrated that better OER catalytic activity could be achieved through the improvement of the electrical conductivity. The intrinsic OER catalytic activities were then analyzed by calculating the surfaces Gibbs free energy (ΔG) profiles of Ni₂P@NPC, FeP@NPC, and Ni₂P/FeP@NPC models through a four-step pathway at alkaline conditions (Figure S10):



where * denotes the active sites on the catalyst surface. As shown in Figure 5a, the ΔG diagrams demonstrated that all electrocatalysts possessed the same rate-determining steps (RDS), which was the formation of the *OOH intermediate in the third step. The Ni₂P/FeP@NPC electrocatalyst displayed the smallest total energy barrier (ΔG : 1.84 eV) compared with the Ni₂P@NPC (2.23 eV) and FeP@NPC (2.75 eV). These results indicated that the formation of the heterointerface could optimize the adsorption and desorption steps in Ni₂P/FeP@NPC to accelerate the whole OER process. As for the HER process, the intrinsic HER activities of the catalysts could be investigated through the Gibbs free energy of hydrogen (ΔG_{H^*}) adsorption. The negative ΔG_{H^*} is beneficial for the adsorption of H* but generates side effects on the desorption of products while too positive ΔG_{H^*} does the opposite. When ΔG_{H^*} is tending to zero, the H* and H₂ are more easily adsorbed and desorbed at the active center, which could be beneficial for the HER. The Ni₂P/FeP@NPC presented the positive ΔG_{H^*} of 0.18 eV (Figure 5d), which was much lower than Ni₂P@NPC (0.79 eV) and FeP@NPC (0.47 eV), confirming that the interaction between Ni₂P/FeP and N, P-doped carbon could adjust the ΔG_{H^*} to zero to facilitate the reaction.

All above theoretical/experimental experiments demonstrated that the fantastic catalytic activities of Ni₂P/FeP@NPC were ascribed to the three-phase heterojunction interface constructed by NPC, Ni₂P and FeP, which could effectively optimize the desorption of intermediates and thus significantly boost the kinetics in OER, HER, and the overall water splitting process. The heterojunction interface optimized the adsorption/desorption ability of intermediates (O*, OH*, OOH* and H*), and the inner Ni₂P/FeP possess superior electrical conductivity and high electron density near the Fermi level, which has better conductivity and a high transfer coefficient, could produce synergistic effects in promoting both HER and OER performance.

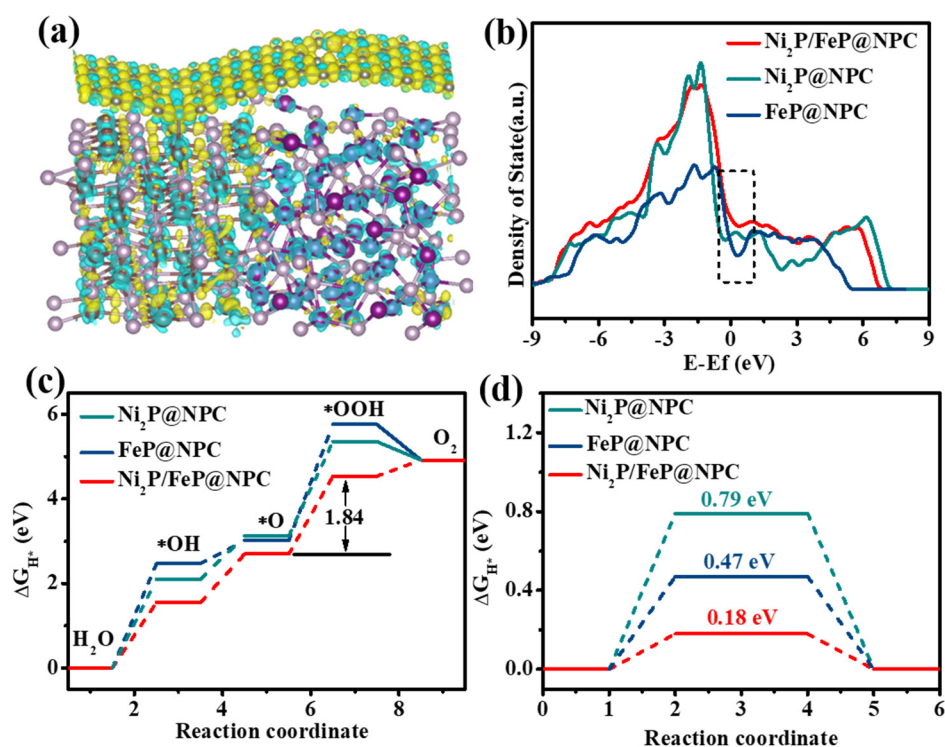


Figure 5. (a) Differential charge density between N, P-doped carbon and Ni₂P/FeP in the heterostructure (gray: C, purple: Ni, brown: Fe, pink: P, orange: N, white: H); (b) The density of states (DOS) of Ni₂P@NPC, FeP@NPC, and Ni₂P/FeP@NPC; (c) The standard free energy diagrams in the OER process of Ni₂P@NPC, FeP@NPC, and Ni₂P/FeP@NPC; (d) Gibbs free energy (DG) profile of the HER on Ni₂P@NPC, FeP@NPC, and Ni₂P/FeP@NPC.

3. Materials and Methods

3.1. Synthesis of MOF Precursors

Typically, STA-12 was synthesized by hydrothermal as early reported. [24] In brief, N, N'-piperazinebis(methylenephosphonic acid) was synthesized using a variation of the modified Mannich reaction of piperazine, using HCl as a catalyst. In a typical synthetic process of Ni-STA-12, nickel acetate tetrahydrate (0.369 g, 0.185 mmol) was stirred together with N, N'-Piperazinebis(methylenephosphonic acid) (0.263 g, 0.93 mmol) in 15 mL deionized water. The pH of the solution was adjusted to 8 by the addition of potassium hydroxide solution. The acidified solution was then placed in a 25 cm³ Teflon-lined autoclave and heated at 160 °C for 48 h. The NiFe-STA-12 or Fe-STA-12 contrasts were synthesized by adjusting the corresponding metal salt, while the other experimental processes and parameters were kept unchanged. The resultant crystalline materials were thoroughly washed with deionized water several times and dried at 80 °C for 12 h under vacuum.

3.2. Synthesis of the Ni₂P@NPC, Ni₂P/FeP@NPC and FeP@NPC

In a typical phosphorization procedure, 500 mg sodium hypophosphite powder was positioned upstream of the tube as the phosphorous source. Subsequently, the as-obtained MOF precursor (100 mg) was positioned at the center of the tube and phosphorized under argon vapor at 450 °C for 2 h. After cooling, the obtained product was denoted Ni₂P@NPC, Ni₂P/FeP@NPC and FeP@NPC, respectively.

4. Conclusions

In summary, the N, P-doped carbon layer-encapsulated Ni₂P/FeP heterojunction nanorods (Ni₂P/FeP@NPC) were successfully engineered and synthesized. As revealed by the DFT results, the electrons could redistribute among the N, P-doped carbon, Ni₂P, and FeP, to optimize the adsorption energy of H- and O-containing intermediates, which endows

the best ΔG_{H^+} for HER and decreases the ΔG of RDS for OER to improve the HER/OER intrinsic activity. The Ni₂P/FeP@NPC exhibited excellent activity for HER ($\eta_{10} = 182$ mV) and OER ($\eta_{10} = 273$ mV), which was much better than Ni₂P@NPC (HER: $\eta_{10} = 214$ mV, OER: $\eta_{10} = 323$ mV) and FeP@NPC (HER: $\eta_{10} = 217$ mV, OER: $\eta_{10} = 330$ mV). Meanwhile, the heterojunction could effectively facilitate electronic transfers at large current density and the carbon layers could avoid metal dissolution in harsh solutions, which makes Ni₂P/FeP@NPC exhibit excellent stability for water splitting. This work provides fantastic catalytic candidates for industrial electrochemical water splitting.

Supplementary Materials: The following supporting information can be downloaded at: <https://www.mdpi.com/article/10.3390/molecules28052280/s1>, Figure S1: Raman patterns of Ni₂P@NPC, Ni₂P/FeP@NPC and FeP@NPC; Figure S2: (a) SEM images of Ni₂P@NPC and (b) FeP@NPC; Figure S3: (a) TEM image of Ni₂P/FeP@NPC and the corresponding EDX element mapping for (b) C, (c) Ni, (d) Fe, (e) P and (f) N; Figure S4: Survey scan of Ni₂P/FeP@NPC; Figure S5: Cyclic voltammograms for Ni₂P@NPC with different scan rates from 10 to 100 mV s⁻¹ in the potential range of 1.1–1.30 V versus RHE; Figure S6: Cyclic voltammograms for FeP@NPC with different scan rates from 10 to 100 mV s⁻¹ in the potential range of 1.1–1.30 V versus RHE; Figure S7: Cyclic voltammograms for Ni₂P/FeP@NPC with different scan rates from 10 to 100 mV s⁻¹ in the potential range of 1.1–1.30 V versus RHE; Figure S8: (a) Survey scan of Ni₂P/FeP@NPC; High-resolution XPS spectra of (b) C, (c) Fe (d) Ni, (e) N and (f) P in Ni₂P/FeP@NPC; Table S1: Comparison of the OER activities with available robust catalysts; Table S2: Comparison of the overall water splitting activities with available robust bifunctional catalysts; Figure S9: Atomic models of (a) Ni₂P@NPC, (b) FeP@NPC and (c) Ni₂P/FeP@NPC (gray: C, purple: Ni, brown: Fe, pink: P, orange: N, white: H); Figure S10: Atomic models of (a), (b) and (c) Ni₂P@NPC, (d), (e) and (f) FeP@NPC and (g), (h) and (i) Ni₂P/FeP@NPC absorbed OH, O and OOH intermediates (gray: C, purple: Ni, brown: Fe, pink: P, orange: N, white: H, red: O).

Author Contributions: H.J.: investigation, visualization, writing—original draft preparation, S.Z. and L.Y.: DFT calculations, Q.F.: XPS spectrum analysis, J.Z. and X.Z.: resources, conceptualization, supervision, funding acquisition, and writing—reviewing. All authors have read and agreed to the published version of the manuscript.

Funding: This work was supported by the National Natural Science Foundation of China (Grant No. 21975286), the project ZR2020QE058 supported by Shandong Provincial Natural Science Foundation, the Colleges and Universities Twenty Terms Foundation of Jinan City (No. 202228053), the QJUT Special Funding for Distinguished Scholars (Grant No. 2419010420).

Institutional Review Board Statement: Not applicable.

Informed Consent Statement: Not applicable.

Data Availability Statement: The data presented are available from the authors.

Conflicts of Interest: The authors declare that they have no conflict of interest.

References

1. Chen, J.; Ren, B.; Cui, H.; Wang, C. Constructing Pure Phase Tungsten-Based Bimetallic Carbide Nanosheet as an Efficient Bifunctional Electrocatalyst for Overall Water Splitting. *Small* **2020**, *16*, 1907556. [[CrossRef](#)] [[PubMed](#)]
2. Sanati, S.; Morsali, A.; Garcia, H. First-row transition metal-based materials derived from bimetallic metal-organic frameworks as highly efficient electrocatalysts for electrochemical water splitting. *Energy Environ. Sci.* **2022**, *15*, 3119–3151. [[CrossRef](#)]
3. Li, C.F.; Zhao, J.W.; Xie, L.J.; Wu, J.Q.; Ren, Q.; Wang, Y.; Li, G.R. Surface-Adsorbed Carboxylate Ligands on Layered Double Hydroxides/Metal-Organic Frameworks Promote the Electrocatalytic Oxygen Evolution Reaction. *Angew Chem. Int. Ed. Engl.* **2021**, *60*, 18129–18137. [[CrossRef](#)] [[PubMed](#)]
4. Zhao, Y.; Liang, Y.; Wu, D.; Tian, H.; Xia, T.; Wang, W.; Xie, W.; Hu, X.M.; Tian, X.; Chen, Q. Ruthenium Complex of sp² Carbon-Conjugated Covalent Organic Frameworks as an Efficient Electrocatalyst for Hydrogen Evolution. *Small* **2022**, *18*, 2107750. [[CrossRef](#)] [[PubMed](#)]
5. Gao, R.; Wang, J.; Huang, Z.-F.; Zhang, R.; Wang, W.; Pan, L.; Zhang, J.; Zhu, W.; Zhang, X.; Shi, C.; et al. Pt/Fe₂O₃ with Pt–Fe pair sites as a catalyst for oxygen reduction with ultralow Pt loading. *Nat. Energy* **2021**, *6*, 614–623. [[CrossRef](#)]
6. Qian, G.; Chen, J.; Yu, T.; Liu, J.; Luo, L.; Yin, S. Three-Phase Heterojunction NiMo-Based Nano-Needle for Water Splitting at Industrial Alkaline Condition. *Nanomicro Lett.* **2021**, *14*, 20. [[CrossRef](#)]

7. Wu, B.; Gong, S.; Lin, Y.; Li, T.; Chen, A.; Zhao, M.; Zhang, Q.; Chen, L. A Unique NiOOH@FeOOH Heteroarchitecture for Enhanced Oxygen Evolution in Saline Water. *Adv. Mater.* **2022**, *34*, 2108619. [[CrossRef](#)]
8. Jiang, H.; Yan, L.; Zhang, S.; Zhao, Y.; Yang, X.; Wang, Y.; Shen, J.; Zhao, X.; Wang, L. Electrochemical Surface Restructuring of Phosphorus-Doped Carbon@MoP Electrocatalysts for Hydrogen Evolution. *Nanomicro Lett.* **2021**, *13*, 215. [[CrossRef](#)]
9. Padha, B.; Verma, S.; Mahajan, P.; Gupta, V.; Khosla, A.; Arya, S. Role of Electrochemical Techniques for Photovoltaic and Supercapacitor Applications. *Crit. Rev. Anal. Chem.* **2022**, 1–35. [[CrossRef](#)]
10. Chai, L.; Hu, Z.; Wang, X.; Xu, Y.; Zhang, L.; Li, T.T.; Hu, Y.; Qian, J.; Huang, S. Stringing Bimetallic Metal–Organic Framework-Derived Cobalt Phosphide Composite for High-Efficiency Overall Water Splitting. *Adv. Sci.* **2020**, *7*, 1903195. [[CrossRef](#)]
11. Hu, H.; Wang, Z.; Cao, L.; Zeng, L.; Zhang, C.; Lin, W.; Wang, C. Metal-organic frameworks embedded in a liposome facilitate overall photocatalytic water splitting. *Nat. Chem.* **2021**, *13*, 358–366. [[CrossRef](#)] [[PubMed](#)]
12. Zhuang, Z.; Wang, Y.; Xu, C.Q.; Liu, S.; Chen, C.; Peng, Q.; Zhuang, Z.; Xiao, H.; Pan, Y.; Lu, S.; et al. Three-dimensional open nano-netcage electrocatalysts for efficient pH-universal overall water splitting. *Nat. Commun.* **2019**, *10*, 4875. [[CrossRef](#)] [[PubMed](#)]
13. Ramesh, S.K.; Son, J.; Ganesan, V.; Kim, J. Carbon-incorporated Ni₂P-Fe₂P hollow nanorods as superior electrocatalysts for the oxygen evolution reaction. *Nanoscale* **2022**, *14*, 16262–16269. [[CrossRef](#)] [[PubMed](#)]
14. Sun, H.; Min, Y.; Yang, W.; Lian, Y.; Lin, L.; Feng, K.; Deng, Z.; Chen, M.; Zhong, J.; Xu, L.; et al. Morphological and Electronic Tuning of Ni₂P through Iron Doping toward Highly Efficient Water Splitting. *ACS Catal.* **2019**, *9*, 8882–8892. [[CrossRef](#)]
15. Wu, L.; Yu, L.; Zhang, F.; McElhenny, B.; Luo, D.; Karim, A.; Chen, S.; Ren, Z. Heterogeneous Bimetallic Phosphide Ni₂P-Fe₂P as an Efficient Bifunctional Catalyst for Water/Seawater Splitting. *Adv. Funct. Mater.* **2021**, *31*, 2006484. [[CrossRef](#)]
16. Du, R.; Wu, Y.; Yang, Y.; Zhai, T.; Zhou, T.; Shang, Q.; Zhu, L.; Shang, C.; Guo, Z. Porosity Engineering of MOF-Based Materials for Electrochemical Energy Storage. *Adv. Energy Mater.* **2021**, *11*, 2100154. [[CrossRef](#)]
17. Yan, L.; Xu, Y.; Chen, P.; Zhang, S.; Jiang, H.; Yang, L.; Wang, Y.; Zhang, L.; Shen, J.; Zhao, X.; et al. A Freestanding 3D Heterostructure Film Stitched by MOF-Derived Carbon Nanotube Microsphere Superstructure and Reduced Graphene Oxide Sheets: A Superior Multifunctional Electrode for Overall Water Splitting and Zn-Air Batteries. *Adv. Mater.* **2020**, *32*, 2003313. [[CrossRef](#)]
18. Pouramini, Z.; Mousavi, S.M.; Babapoor, A.; Hashemi, S.A.; Lai, C.W.; Mazaheri, Y.; Chiang, W.-H. Effect of Metal Atom in Zeolitic Imidazolate Frameworks (ZIF-8 & 67) for Removal of Dyes and Antibiotics from Wastewater: A Review. *Catalysts* **2023**, *13*, 155. [[CrossRef](#)]
19. Annamalai, J.; Murugan, P.; Ganapathy, D.; Nallaswamy, D.; Atchudan, R.; Arya, S.; Khosla, A.; Barathi, S.; Sundramoorthy, A.K. Synthesis of various dimensional metal organic frameworks (MOFs) and their hybrid composites for emerging applications—A review. *Chemosphere* **2022**, *298*, 134184. [[CrossRef](#)]
20. Doustkhah, E.; Hassandoost, R.; Khataee, A.; Luque, R.; Assadi, M.H.N. Hard-templated metal-organic frameworks for advanced applications. *Chem. Soc. Rev.* **2021**, *50*, 2927–2953. [[CrossRef](#)]
21. Feng, L.; Wang, K.Y.; Yan, T.H.; Zhou, H.C. Seed-mediated evolution of hierarchical metal-organic framework quaternary superstructures. *Chem. Sci.* **2020**, *11*, 1643–1648. [[CrossRef](#)] [[PubMed](#)]
22. Lu, X.F.; Fang, Y.; Luan, D.; Lou, X.W.D. Metal-Organic Frameworks Derived Functional Materials for Electrochemical Energy Storage and Conversion: A Mini Review. *Nano Lett.* **2021**, *21*, 1555–1565. [[CrossRef](#)] [[PubMed](#)]
23. Radwan, A.; Jin, H.; He, D.; Mu, S. Design Engineering, Synthesis Protocols, and Energy Applications of MOF-Derived Electrocatalysts. *Nanomicro Lett.* **2021**, *13*, 132. [[CrossRef](#)] [[PubMed](#)]
24. Groves, J.A.; Miller, S.R.; Warrender, S.J.; Mellot-Draznieks, C.; Lightfoot, P.; Wright, P.A. The first route to large pore metal phosphonates. *Chem. Commun.* **2006**, *31*, 3305–3307. [[CrossRef](#)]
25. Bai, L.; Pang, X.; Sun, Y.; Zhang, X.; Guo, J. N-doped graphene wrapped SnP₂O₇ for sodium storage with high pseudocapacitance contribution. *J. Alloy Compd.* **2021**, *854*, 156992. [[CrossRef](#)]
26. Feng, Y.; Xu, C.; Hu, E.; Xia, B.; Ning, J.; Zheng, C.; Zhong, Y.; Zhang, Z.; Hu, Y. Construction of hierarchical FeP/Ni₂P hollow nanospindles for efficient oxygen evolution. *J. Mater. Chem. A* **2018**, *6*, 14103–14111. [[CrossRef](#)]
27. Tan, L.; Yu, J.; Wang, C.; Wang, H.; Liu, X.; Gao, H.; Xin, L.; Liu, D.; Hou, W.; Zhan, T. Partial Sulfidation Strategy to NiFe-LDH@FeNi₂S₄ Heterostructure Enable High-Performance Water/Seawater Oxidation. *Adv. Funct. Mater.* **2022**, *32*, 2200951. [[CrossRef](#)]
28. Yang, M.; Xie, J.-Y.; Lin, Z.-Y.; Dong, B.; Chen, Y.; Ma, X.; Wen, M.-L.; Zhou, Y.-N.; Wang, L.; Chai, Y.-M. N-doped FeP nanorods derived from Fe-MOFs as bifunctional electrocatalysts for overall water splitting. *Appl. Surf. Sci.* **2020**, *507*, 145096. [[CrossRef](#)]

Disclaimer/Publisher’s Note: The statements, opinions and data contained in all publications are solely those of the individual author(s) and contributor(s) and not of MDPI and/or the editor(s). MDPI and/or the editor(s) disclaim responsibility for any injury to people or property resulting from any ideas, methods, instructions or products referred to in the content.